Direct Numerical Simulation of a Fully Developed Turbulent Channel Flow With Respect to the Reynolds Number Dependence

Hiroyuki Abe

Hiroshi Kawamura

Department of Mechanical Engineering,
Science University of Tokyo,
Noda-shi, Chiba, 278-8510, Japan

Yuichi Matsuo

National Aerospace Laboratory,
Chofu-shi, Tokyo, 182-8522, Japan

Direct numerical simulation (DNS) of a fully developed turbulent channel flow for various Reynolds numbers has been carried out to investigate the Reynolds number dependence. The Reynolds number is set to be $Re_\tau=180$, 395, and 640, where Re_τ is the Reynolds number based on the friction velocity and the channel half width. The computation has been executed with the use of the finite difference method. Various turbulence statistics such as turbulence intensities, vorticity fluctuations, Reynolds stresses, their budget terms, two-point correlation coefficients, and energy spectra are obtained and discussed. The present results are compared with the ones of the DNSs for the turbulent boundary layer and the plane turbulent Poiseuille flow and the experiments for the channel flow. The closure models are also tested using the present results for the dissipation rate of the Reynolds normal stresses. In addition, the instantaneous flow field is visualized in order to examine the Reynolds number dependence for the quasi-coherent structures such as the vortices and streaks. [DOI: 10.1115/1.1366680]

Introduction

With the aid of recent developments in the super and parallel computers, the direct numerical simulation (DNS, hereafter) of turbulence is now being increasingly performed.

The DNS is a time-dependent and three-dimensional numerical solution in which the governing equations are computed as accurately as possible without any turbulence models introduced. The DNS provides various information, such as velocity, pressure, and their derivatives at any time and point in the instantaneous flow field. These are extremely difficult to be measured in experiments. The first attempt of the DNS was made by Orszag and Patterson [1] 25 years ago for a homogeneous turbulence. For the wall turbulence, the DNS of the fully developed turbulent channel flow started more recently. It was, however, more than 10 years ago when Kim et al. [2] (KMM87, hereafter) published their DNS on the turbulent channel flow. Their Reynolds number based on the friction velocity u_τ and the channel half width δ was $Re_\tau=180$. Since then, the DNS of the turbulent channel flow has often been performed because of its simple geometry and fundamental nature to understand the transport mechanism. Kuroda et al. [3] and Kasagi et al. [4] carried out the DNS for a slightly lower Reynolds number of $Re_\tau=150$. Kim et al. [5] (KMM90, hereafter) also performed a DNS with a higher Reynolds number of $Re_\tau=395$. Antonia and Kim [6] analyzed the DNS data by KMM87 [2] and KMM90 [5] and obtained various turbulence quantities in the near-wall region. They found that the Reynolds-number effect on the turbulence quantities was rather significant. However, it is not known yet whether this non-negligible dependence on the Reynolds number could be extrapolated to a higher Reynolds number or not. The authors group (Kawamura et al. [7]; Kawamura et al. [8]) performed the DNS to include the scalar transport with various Prandtl numbers for $Re_\tau=180$ and 395. They carried out the DNS also for a higher Reynolds number of $Re_\tau=640$ and reported preliminary results in Kawamura [9] and Kawamura et al. [10]. Meanwhile the calculation was extended further; the present paper reports the detailed results. Quite recently, Moser et al. [11] pub-

lished a brief communication on their DNS for a slightly lower Reynolds number of $Re_\tau=590$. Their results are also included in this paper for comparison.

Extensive effort has been devoted to the experimental study of the turbulent channel flow. Laufer [12] first obtained the detailed turbulence statistics in the channel flow at three Reynolds numbers of $Re_c=12,300$, 30,800, and 61,600, where Re_c is the Reynolds number based on the centerline velocity u_c and the channel half width. Later, Hussain and Reynolds [13] reported the higher-order turbulence quantities with the use of an extremely long channel for $Re_c=13,800-33,300$. Kreplin and Eckelmann [14] made their experiments with the hot-film measurement for low Reynolds numbers of $Re_c=2800-4100$. Johansson and Alfredsson [15] carried out the experiment with the hot-film probes in a water channel for $Re_c=6900-24,450$, focusing on the Reynolds-number effect. Wei and Willmarth [16] performed an experiment with the laser-Doppler anemometer in a water channel for $Re_c=3000-40,000$ to investigate the existence of an inner scaling law. Recently, Antonia et al. [17] made velocity measurement using the X-wire for $Re_c=3300-21,500$ and also carried out the DNS for $Re_c=3300$, and 7900. They examined the Reynolds number dependence concentrating mainly on the inner region. Although a large amount of knowledge was accumulated through the experiments, there existed always some discrepancies among the existing experimental results, especially in the near-wall region. More recently, Nishino and Kasagi [18,19] carried out the measurement by the three-dimensional particle tracking velocimeter method (PTV, hereafter) at a low Reynolds number of $Re_\tau=205$ ($Re_c=3755$). They obtained a good agreement with the DNS of KMM87 [2] including the near-wall region.

In the present work, the DNS of turbulent channel flow has been carried out with the use of the finite difference method. The Reynolds number is set to be $Re_\tau=180$, 395, and 640. For $Re_\tau=180$ and 395, the obtained results are compared with those of KMM87 [2] and KMM90 [5] to show the reliability of the present numerical method. On the other hand, Moin and Kim [20] carried out a large eddy simulation for $Re_\tau=640$ more than 10 years ago to compare the results with the experiment of Hussain and Reynolds [13]. The present computation is also executed for $Re_\tau=640$ based on that of Kawamura et al. [10], which is, to the authors' knowledge, the highest Reynolds number ever simulated through DNS for this configuration. Various turbulence statistics

---

Copyright © 2001 by ASME

Table 1 Spatial resolution

Re_τ	180	395	640
Computational volume (x,y,z)	$12.8\delta \times 2\delta \times 6.4\delta$	$6.4\delta \times 2\delta \times 3.2\delta$	$6.4\delta \times 2\delta \times 2\delta$
Computational volume (x^+,y^+,z^+)	$2304 \times 360 \times 1152$	$2528 \times 790 \times 1264$	$4096 \times 1280 \times 1280$
Grid number	$256 \times 128 \times 256$	$256 \times 192 \times 256$	$512 \times 256 \times 256$
Spatial resolution $(\Delta x^+, \Delta z^+)$	9.00, 4.50	9.88, 4.94	8.00, 5.00
Spatial resolution (Δy^+)	0.20~5.90	0.20~9.64	0.15~8.02
Time integration (t^+)	4,320	15,800	24,800

such as turbulence intensities, vorticity fluctuations, Reynolds stresses, their budget terms, two-point correlation coefficients, and energy spectra are examined to investigate the Reynolds-number dependence in detail.

Computational Domain

The DNS must meet the following two requirements to ensure the adequacy of the computation. One is that the computational domain must be chosen to be large enough to contain the largest eddies. The other is that the grid spacing must be fine enough to resolve the smallest eddies. The former is confirmed if the two-point correlation becomes zero within a half of the computational domain. Recently, Jiménez [21] pointed out that the product of the wave number and the one-dimensional spectrum serves also as a good measure of the computational domain. The latter can be satisfied if the one-dimensional energy spectra shows enough drop-offs for the high wave numbers. The present computation takes into account the above requirements, although a rather smaller volume is selected to save the computational storage. The flow is assumed to be fully developed in an infinite two-dimensional channel. The mean flow is in x direction and is driven by a streamwise mean pressure gradient. Note that x (x_1), y (x_2), and z (x_3) imply streamwise, wall-normal and spanwise directions, respectively. The periodic boundary condition is imposed in x and z directions, while nonslip condition is adopted on the top and bottom walls. The uniform meshes are used in the x and z directions. On the other hand, the nonuniform meshes are adopted in the y direction. The transformation is similar to that of Moin and Kim [20] as

$$y_j = \frac{1}{2\alpha} \tanh[\xi_j \tanh^{-1} \alpha] + 0.5, \qquad (1)$$

with

$$\xi_j = -1 + 2\frac{j}{N_2}, \qquad (2)$$

where α is an adjustable parameter of the transformation ($0 < \alpha < 1$) and N_2 is the grid number of the y direction. In the case of $Re_\tau = 180$ and 395, a constant value of $\alpha = 0.967$ and 0.980 are adopted, respectively. On the other hand, in the case of $Re_\tau = 640$, a function is employed for the parameter α

$$\alpha(\xi_j) = 0.9885 - 0.5\xi_j^2 + 0.405\xi_j^3. \qquad (3)$$

The computational condition is shown in Table 1. Note that the superscript $+$ indicates the quantities normalized by the wall variables, e.g., $y^+ = yu_\tau/\nu$ and $t^+ = tu_\tau^2/\nu$. For the highest Reynolds number for $Re_\tau = 640$, the computation has been executed on 33, 554, 432 ($512 \times 256 \times 256$) grid points to resolve the smallest eddies.

Numerical Procedures

The coordinates and flow variables are normalized by the channel half width δ, the kinematic viscosity ν, and the friction velocity $u_\tau = (\tau_w/\rho)^{1/2}$, where τ_w is the statistically averaged wall shear stress and ρ is the density.

The fundamental equations are the continuity equation:

$$\frac{\partial u_i^+}{\partial x_i^*} = 0, \qquad (4)$$

and the Navier-Stokes equation:

$$\frac{\partial u_i^+}{\partial t^*} + u_j^+ \frac{\partial u_i^+}{\partial x_j^*} = -\frac{\partial p^+}{\partial x_i^*} + \frac{1}{Re_\tau}\frac{\partial^2 u_i^+}{\partial x_j^{*2}} + \frac{\partial \bar{p}^+}{\partial x_1^*}\delta_{il}. \qquad (5)$$

Here, $i = 1$, 2, and 3 indicate the streamwise, wall-normal, and spanwise directions, respectively. The variables t and p are the time and the pressure. The superscript $*$ indicates that the variables are normalized by δ. Note that the third term for the right-hand side of Eq. (5) is the streamwise mean pressure gradient.

The boundary conditions are

$$u_i^+ = 0, \quad \text{at } y = 0 \quad \text{and} \quad 2\delta. \qquad (6)$$

In the present computation, fractional step method proposed by Dukowics and Dvinsky [22] is adopted for the computational algorithm. Time advancement is executed by the semi-implicit scheme: Crank-Nicolson method for the viscous terms (wall-normal direction) and Adams-Bashforth method for the other terms.

For spatial discretization, the finite difference method (FDM, hereafter) is adopted. In the preceding DNSs, the pseudo-spectral method (PSM, hereafter) has been often preferred because a higher-numerical accuracy can be obtained for a given grid size through PSM than through FDM. On the other hand, the FDM has a potential to be applied to more complex geometries and spatially developing flow in future works; thus it is considered to be worthwhile to verify an applicability of the FDM to DNS in comparison with existing PSM results. Several DNSs have been performed with the use of FDM by Rai and Moin [23,24] for turbulent channel and boundary layer and by Gavrilakis [25] for square duct.

In the early stage of the present work, a series of computations, were made in which DNSs of the fully developed turbulent channel flow were performed with various discretization methods including the upwind and the second- and fourth-order central schemes (Kawamura [26]; Suzuki and Kawamura [27]).

As for the transport equation for the turbulent kinetic energy and the Reynolds stresses, the use of the upwind scheme showed an underestimation of the dissipation rate due to the numerical viscosity in the transportation of the turbulent kinetic energy and the Reynolds stresses. Even in the computation with the use of the central scheme, the sum of the all terms in those transport equations never tended to fall to zero. It was noticed that this was due to the inconsistency between the numerical and analytical differential operations employed in solution of the momentum and transport equations.

The obtained conclusions can be summarized as follows. The transport equation of the Reynolds stresses is derived from the momentum equation through a lot of differential operations using the continuity condition. In the calculation of DNS, the momentum equation must be solved with a sufficient accuracy corresponding to the order of applied discretization. Thus, if ever a significant residual remains in the sum of the terms in the Reynolds stress transport equations, it is because the numerical differentiation scheme is not consistent with the analytical one. The inconsistency was pointed out first by Schumann [28] more than

Table 2 Mean flow variables

Re_τ	u_m	u_c	u_c/u_m	Re_m	Re_c	Re_θ	C_f
180	15.72	18.38	1.17	5662	3309	295	8.11×10^{-3}
395	17.70	20.48	1.16	13981	8090	754	6.39×10^{-3}
640	19.00	21.85	1.15	24326	13984	1283	5.50×10^{-3}

twenty years ago. The authors group (Kawamura [26]; Suzuki and Kawamura [27]) extended this idea to apply to DNS. The resultant scheme was called the ''consistent scheme'' because of its consistency between the numerical and analytical difference operations. It was originally with the second-order accuracy. Some more details are given in the Appendix. Later, Kajishima [29] and Morinishi [30] extended it into the fourth-order one. The present computation has been executed with the second-order scheme; while the fourth-order scheme is also tested and compared in the Appendix. As for the computational stencil, the staggered grid is adopted; that is, the pressure is located at the cell center and the velocities at the cell surfaces.

The Poisson equation of pressure is solved using the tridiagonal matrix algorithm in the wall-normal direction and the fast Fourier transform (FFT) in the streamwise and the spanwise directions with the use of the second-order scheme. For the viscous terms, the second-order central scheme is used.

The computer employed is NWT (Numerical Wind Tunnel) located at the National Aerospace Laboratory. It is a vectorized parallel computer with 166 processor elements, connected through the cross bar network of 421 MB/s. The computation speed of each processor is 1.7 GFLOPS, thus the theoretical maximum performance of the whole system is 280 GFLOPS. In case of the highest Reynolds number of $Re_\tau=640$, the computation has been made using of 64 processors with the typical integration time of about 1.4 s for a time step. The calculation has been executed up to 24,800 ν/u_τ^2 in order to obtain a stable statistical average.

Results and Discussion

Mean Flow Variables. Mean flow variables such as the bulk mean velocity u_m, the mean centerline velocity u_c, the Reynolds numbers Re_m, Re_c, and Re_θ and the friction coefficient C_f are given in Table 2 for the three Reynolds numbers. Here, Re_m is the Reynolds number based on the bulk mean velocity and the channel width and Re_c is the one based on the mean centerline velocity and the channel half width. Note that Re_θ is based on the mean centerline velocity and the momentum thickness. In the present case, the momentum thickness θ is defined as

$$\frac{\theta}{\delta} = \int_0^1 \frac{\bar{u}^+}{\bar{u}_c^+}\left(1 - \frac{\bar{u}^+}{\bar{u}_c^+}\right)dy^*. \tag{7}$$
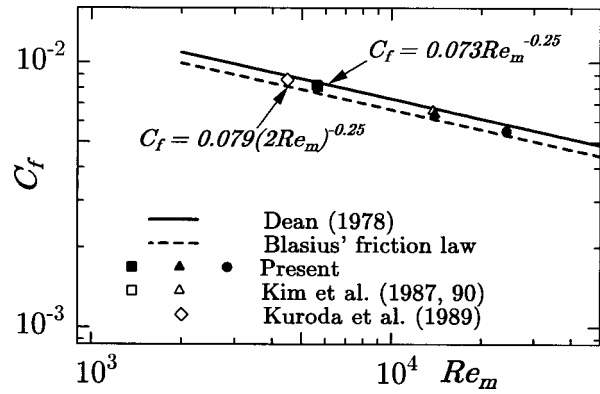
In the case of $Re_\tau=640$, Re_θ is about 10 percent lower than that of the DNS with $Re_\theta=1410$ by Spalart [31] for the turbulent boundary layer; while, u_c for $Re_\tau=640$ is roughly equivalent to u_∞ for $Re_\theta=1410$ by Spalart [31], where u_∞ is the edge velocity. The present results also agree with the correlation between the bulk mean velocity and the mean centerline velocity proposed by Dean [32]:

$$u_c/u_m = 1.28\,Re_m^{-0.0116}. \tag{8}$$

The friction coefficient is defined as

$$C_f = \tau_w \Big/ \left(\frac{1}{2}\rho u_m^2\right), \tag{9}$$

where τ_w is the wall shear stress. Figure 1 shows the friction coefficient in comparison with those of DNS by Kuroda et al. [3] and KMM87 [2]. There included are the empirical correlation proposed by Dean [32] for the channel flow and the one by Blasius for the pipe flow. The present results are in good agreement

Fig. 1 Friction coefficient

with them. However, there exists a small but discernible difference between the present and the KMM87 [2] and KMM90 [5] results. This is a reflection of the slight difference in the mean velocity distribution in the channel center region.

The mean velocity distribution is given in Fig. 2 and compared with the experiment of Hussain and Reynolds [13]. The DNS of turbulent channel flow by KMM87 [2] and KMM90 [5] and the one of the turbulent boundary layer by Spalart [31] are also included for comparison. The present result for $Re_\tau=640$ is in good agreement with the experiment by Hussain and Reynolds [13]; while a slight deviation from $Re_\theta=1410$ by Spalart [31] is found in the logarithmic region. This is due to a characteristic difference between the channel and the boundary layer flows.
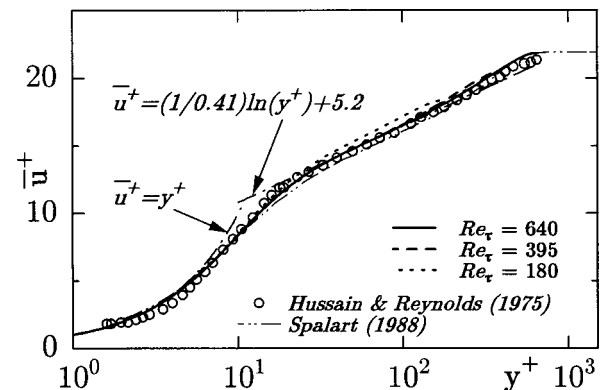
KMM87 [2] pointed out that the logarithmic region exists even in the case of the lowest Reynolds number of 180; while it extends up to a larger y^+ with the increase of Re_τ. Moreover, the wake region is more clearly distinguished from the logarithmic one in the case of the higher Re_τs.

It is well-recognized that the logarithmic region can be expressed as

$$\bar{u}^+ = \frac{1}{\kappa}\ln y^+ + c, \tag{10}$$

where κ is the von Karman constant and c is the additive constant. Note that an overline denotes an average over x, z, and t. In the turbulent boundary layer, Spalart [31] indicated that the result for the higher Reynolds number of $Re_\theta=1410$ gave $\kappa=0.41$ and $c=5.0$. In the case of $Re_\tau=180$, the additive constant c is 5.5, which is in good agreement with that of KMM87 [2]; while in the case of $Re_\tau=640$, the one by the present DNS decreases down to 5.2.

The von Karman constant κ can be obtained from Eq. (10) as

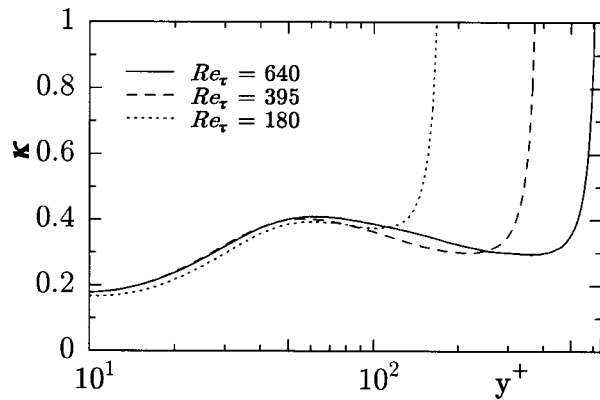**Fig. 2 Mean velocity distribution**

Fig. 3 Von Karman constant

$$\kappa = \left(y^+ \frac{d\bar{u}^+}{dy^+} \right)^{-1} \tag{11}$$

and is plotted in Fig. 3. It is well-known that κ obtained from the experiments ranges from 0.40–0.42. The present calculation indicates that κ is not completely constant but it stays at a roughly constant value of 0.40 around $y^+ = 50 - 100$. Moreover, the region of the approximate constant tends to expand with the increase of the Reynolds number.

Turbulence Intensities. The root mean square of velocity fluctuations is shown in Fig. 4. Those of Moser et al. [11] and u'^+_{rms} of Hussain and Reynolds [13] are also plotted for comparison. All components increase with the increase of Re_τ. Antonia et al. [17] indicated that the Reynolds number dependence for w'^+_{rms} is significant compared to that for u'^+_{rms} and v'^+_{rms}. In the present results, not only w'^+_{rms} but also v'^+_{rms} is enhanced with increasing Reynolds number. Especially, the wall-normal and spanwise components are enhanced. This is because the energy redistribution increases remarkably for v'^+_{rms} and w'^+_{rms} with the increase of the Reynolds number, as will be discussed later. In Fig. 4, the present result shows good agreement with the measurement by Hussain and Reynolds [13] for u'^+_{rms} except for the peak value. This discrepancy may also be caused by the difficulty in the measurement close to the wall. The slight difference between the present (Re_τ=640) and Moser et al. [11] (Re_τ=590) is due to the difference in Re_τ. If they are plotted versus y/δ instead of y^+, the agreement is improved for the central region. In addition, the present results for Re_τ=180 and 395 agree with those of Moser et al. [11].

The root mean square of vorticity fluctuations normalized by the wall variables, i.e., $\omega'_i \nu / u_\tau^2$ are shown in Fig. 5. The near-wall values of streamwise and spanwise vorticity fluctuations ω'^+_x and ω'^+_z increase with the increase of the Reynolds number. Especially, ω'^+_z shows a larger value for a higher Reynolds number. This is caused by the simple shear close to the wall. The wall values of ω'^+_x and ω'^+_z correspond to the coefficients b_3 and b_1, respectively, given in Table 3. The wall-normal vorticity fluctuation ω'^+_y, however, tends to become independent of the Reynolds number in the near-wall region as reported by Antonia and Kim [6].

Reynolds Shear Stress. The Reynolds shear stress $-\overline{u'^+ v'^+}$ and the total shear stress τ_{total} are shown in Fig. 6. As the Reynolds number increases, the peak value of the Reynolds shear stress $-\overline{u'^+ v'^+}$ increases and its position moves away from the wall. When Re_τ is 180, the peak of $-\overline{u'^+ v'^+}$ reaches 0.71 at $y^+=30$; while, in the case of Re_τ=640, it becomes 0.87 at y^+
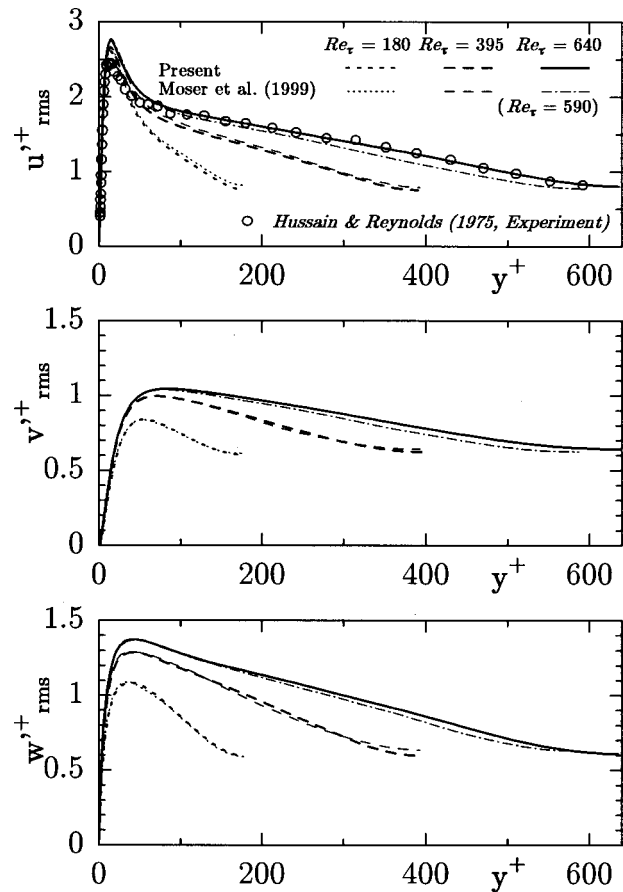

Fig. 4 Rms of velocity fluctuations

=42. On the other hand, the position of the peak moves closer to the wall with the increase of the Reynolds number if scaled by the channel half width δ.

The total shear stress is an identification that the calculation reaches a statistically steady state. When the streamwise momentum equation is ensemble averaged, the total shear stress can be obtained as

$$\tau_{total} = 1 - \frac{y^+}{Re_\tau} = -\overline{u'^+ v'^+} + \frac{\partial \bar{u}^+}{\partial y^+}. \tag{12}$$

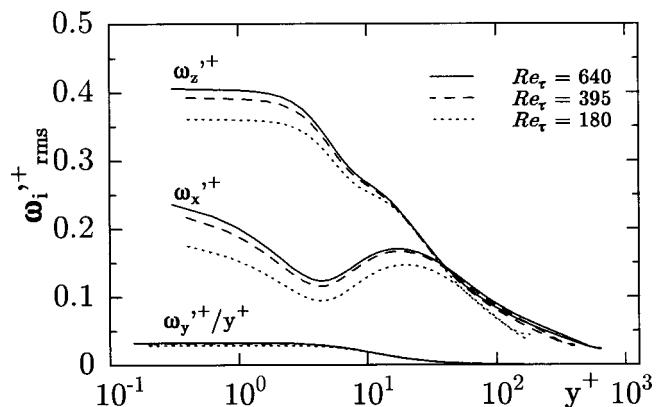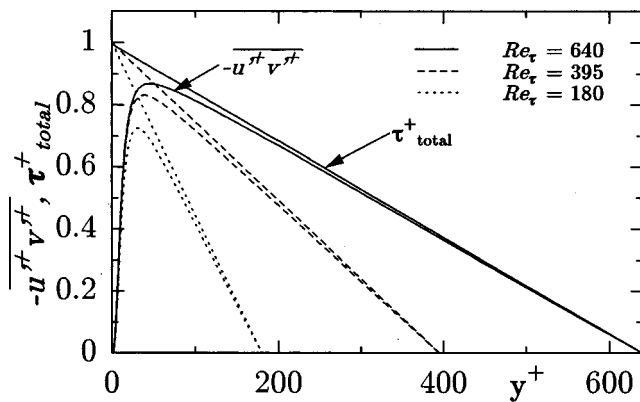Once the statistically steady state is reached, the right and left-

Fig. 5 Rms of vorticity fluctuations

Fig. 6 Reynolds shear stress and total shear stress distributions

hand sides of Eq. (12) must be balanced. In the present DNS, the statistically steady state can be confirmed for all the three Reynolds numbers, as seen in Fig. 6.

Near-Wall Behavior. In the wall vicinity, the velocity fluctuations can be expanded in terms of y^+ as

$$u'^+ = b_1 y^+ + c_1 y^{+2} + \cdots, \tag{13}$$

$$v'^+ = c_2 y^{+2} + \cdots, \tag{14}$$

$$w'^+ = b_3 y^+ + c_3 y^{+3} + \cdots. \tag{15}$$

Considering the expansion of Eqs. (13) and (14), the Reynolds shear stress can be expanded in terms of y^+ as

$$-\overline{u'^+ v'^+} = -\overline{b_1 c_2} y^{+3} + \cdots. \tag{16}$$

The wall-values of b_1, c_2, b_3, and $\overline{b_1 c_2}$ are extrapolated up to the wall and given in Table 3 in comparison with Antonia and Kim [6]. The present results agree well with those of Antonia and Kim [6] in the near-wall region. A discrepancy can be observed for $\overline{b_1 c_2}$. This seems to be caused by the location of the first grid point and the staggered arrangement of the variables in this work. In addition, the present results indicate that the coefficients of b_1, c_2, b_3, and $\overline{b_1 c_2}$ increase with the increase of the Reynolds number. This is because the production rate of the turbulent kinetic energy increases with the increasing Reynolds number as discussed later. Especially, the increase is significant when the Reynolds number goes up from $Re_\tau = 180$–395. In the case of $Re_\tau = 640$, however, the increase is rather saturated. This indicates that the low Reynolds-number effect is significant for $Re_\tau = 180$.

As for the wall-limiting value of b_1 or ω_z', a great deal of effort have been devoted to reaching a consensus through the DNS and experiment. However, there exists long discussion on the quantity because of the experimental difficulties associated with the measurements. Recently, Alfredsson and Johansson [33] carried out the measurements in the air, oil, and water with the hot-film probes and specially designed sensors. They indicated that the rms of the velocity shear stress fluctuation in the streamwise direction is 40 percent of the mean-shear stress for both the channel and the

Table 3 Near-wall expansion coefficient

Re_τ	b_1	c_2	b_3	$b_1 c_2$
180 (Present)	0.361	9.4×10^{-3}	0.199	7.9×10^{-4}
180 (Antonia and Kim [6])	0.356	8.5×10^{-3}	0.190	7.0×10^{-4}
395 (Present)	0.395	1.1×10^{-2}	0.247	1.0×10^{-3}
395 (Antonia and Kim [6])	0.395	1.1×10^{-2}	0.245	9.5×10^{-4}
640 (Present)	0.409	1.2×10^{-2}	0.261	1.1×10^{-3}

boundary layer flows. This corresponds to $b_1 = 0.40$ in the present definition. Komminaho et al. [34] computed the plane turbulent Couette flow at a Reynolds number of 750 based on half the velocity difference between the walls and half the channel width. They indicated a value of $b_1 = 0.41$ at the wall. This is in good accordance with the present value of $b_1 = 0.409$ for $Re_\tau = 640$. In the case of the Couette flow, the total shear stress is constant independent upon the Reynolds number. This is equivalent to the Poiseuille flow with an infinite Re_τ (see Eq. (12)). These indicate that the decrease in b_1 with decreasing Re_τ found in Table 3 is due to the reduction of the total shear stress for the smaller Re_τ in the wall vicinity.

Two-Point Correlations. Streamwise and spanwise two-point correlations of velocity fluctuations $R_{(ii)}$ for $Re_\tau = 640$ are shown in Fig. 7. No summation rule is applied to the parenthesized indices. In the near-wall region, all of the three components tend to fall off to almost zero within a half width of the computational domain for both the streamwise and spanwise directions. Moving away from the wall, however, the spanwise two-point correlation R_{11} gives a small but noticeable deviation from zero even at the half of the spanwise computational domain. This means that there exist the large scale structures in the center of the channel and that the present computational domain is not enough large to capture some of the largest scale ones. Recently, Jiménez [21] investigated the large scale structures in the center of the channel and indicated that even the computational domain adopted by Moser et al. [11] is too short to contain the large scale ones. The large scale structures were also found by Komminaho et al. [34] in the Couette flow. They observed streamwise structures of the order of 40δ in the center of the channel. The above large structures will be investigated with the use of the energy spectra and be discussed later.

The spanwise two-point correlation R_{11} is given in Fig. 8 and compared with the experiment by Nishino and Kasagi [19]. It is interesting to note that the near-wall negative peak of the spanwise R_{11} becomes less prominent with the increase of Re_τ. This is in accordance with the observation that the streamwise streaks are clustered in higher Reynolds number as discussed later.

Energy Spectra. One-dimensional energy spectra of velocity fluctuations $E_{(ii)}$ in the near-wall region for $Re_\tau = 640$ compared with that for $Re_\tau = 180$ are shown in Fig. 9, where k_x and k_z are the wave numbers in the streamwise and spanwise directions, respectively. Note that $E_{(ii)}$ is normalized by the wall units. The energy spectra show acceptable drop-offs in the streamwise and spanwise directions irrespective of the Reynolds number, although a slight pile-up is seen for the highest wave numbers in the spanwise direction. A large difference among three components is observed in the lower wave number region for both the streamwise and spanwise directions. Especially, the difference is significant for the spanwise energy spectra. This indicates that the turbulence structure for the near-wall region becomes more anisotropic in space than the one for the channel center. Moreover, E_{vv} and E_{ww} exhibit noticeable increase in the lower wave number with increasing Reynolds number for both the streamwise and spanwise directions, which is in good accordance with the increase in v'^+_{rms} and w'^+_{rms}.

To investigate whether or not the smallest eddies are resolved, Fig. 10 shows $k_x^2 E_{uu} (\varepsilon^3/\nu)^{-1/4}$ referring to Saddoughi and Veeravalli [35], which represents the energy spectra of the turbulence dissipation rate. In the present result, its peak value occurs at $k_x/k_d = 0.1$–0.2 and falls off for $k_x/k_d > 0.5$ roughly irrespective of the Reynolds number. This corresponds to the well-known fact that the small scale eddies dissipate the energy at a lower wave number than the Kolmogorov scale (Tennekes and Lumley [36]). Although, over $k_x/k_d = 0.2$, some difference is found between the present result and that by PSM (Moser et al. [11]), those higher
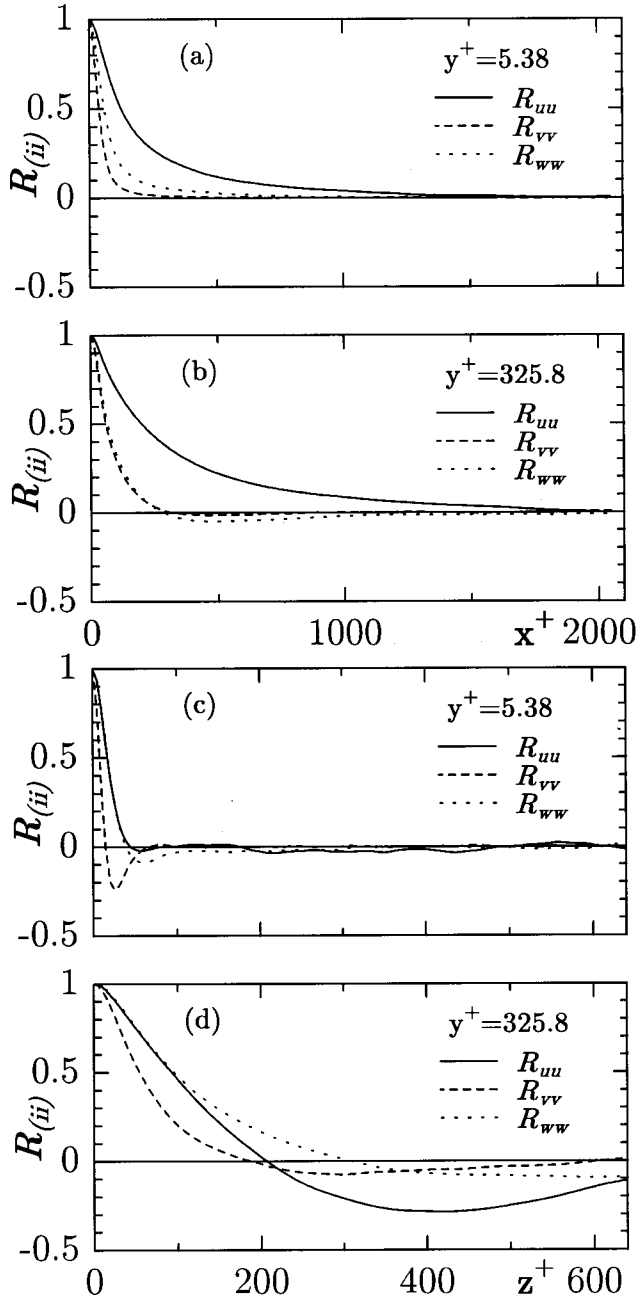
Fig. 7 Two-point correlation coefficients of velocity fluctuations for $Re_\tau = 640$: (a), (b) streamwise, (c), (d) spanwise correlation coefficients

Fig. 8 Spanwise two-point correlation coefficient R_{11} at $y^+ = 11$

wave numbers are less effective for the turbulence statistics. This means that the present spatial resolution is sufficiently small to resolve the energy dissipative eddies.

To show the validity of the adopted computational domain, Figs. 11(a) and 11(b) show the premultiplied energy spectra $k_x E_{uu} / \overline{u'u'}$ and $k_z E_{uu} / \overline{u'u'}$, respectively, referring to Jiménez [21]. In the near-wall region, the peak of $k_z E_{uu} / \overline{u'u'}$ occurs at $\lambda_z^+ \simeq 100$ independent of the Reynolds number, which agrees with the well-known average spacing of the streamwise streak structures. On the other hand, that of $k_x E_{uu} / \overline{u'u'}$ arises at $\lambda_z^+ \simeq 1000$. These correspond to the formation of the streaks as shown later (see Figs. 16 and 17).

In the center of the channel, however, the peak of $k_z E_{uu} / \overline{u'u'}$ moves toward a larger λ_z^+; i.e., $\lambda_z^+ \simeq 1000$ as indicated by Jimé-
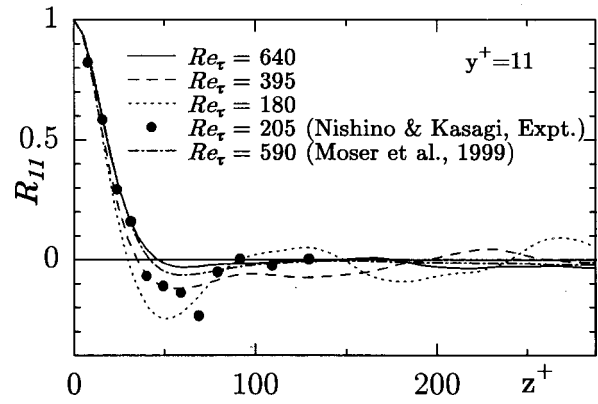
nez [21]. On the other hand, that of $k_x E_{uu} / \overline{u'u'}$ stays at $\lambda_x^+ \simeq 1000$. This means that the spanwise structure is enlarged with the increase of y^+. In the present computation for $Re_\tau = 640$, the peak of $k_z E_{uu} / \overline{u'^+ u'^+}$ cannot be obtained at the center of the channel. This indicates that the largest scale has not been captured totally at the central region of the channel for $Re_\tau = 640$. The present authors are now performing another computation with an extended domain for streamwise and spanwise directions. The preliminary results indicate that its effect on the fundamental turbulent statistics is sufficiently small.

Budget of Reynolds Stress $\overline{u_i' u_j'}$ and Turbulent Kinetic Energy k. Budget terms of Reynolds stress $\overline{u_i' u_j'}$ normalized by ν / u_τ^4 are expressed as follows:

$$\text{Production:} \quad P_{ij} = -\left(\overline{u_j'^+ u_k'^+} \frac{\partial \bar{u}_i^+}{\partial x_k^+} + \overline{u_i'^+ u_k'^+} \frac{\partial \bar{u}_j^+}{\partial x_k^+} \right), \tag{17}$$

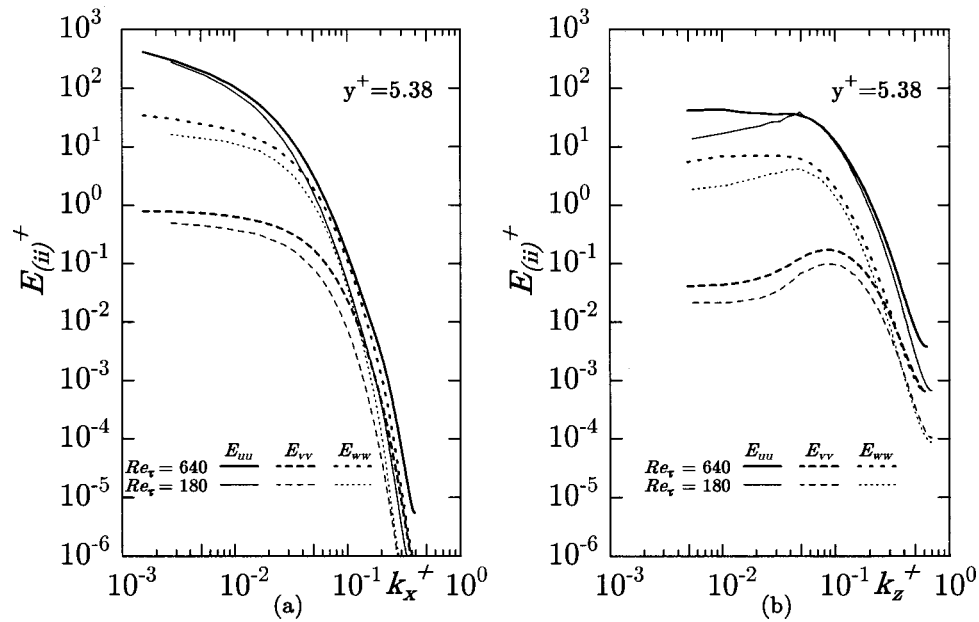$$\text{Turbulent diffusion:} \quad T_{ij} = -\frac{\partial}{\partial x_k^+} (\overline{u_i'^+ u_j'^+ u_k'^+}), \tag{18}$$

$$\text{Vel. p. -grad. corr.:} \quad \Pi_{ij} = -\left(\overline{u_j'^+ \frac{\partial p'^+}{\partial x_i^+}} + \overline{u_i'^+ \frac{\partial p'^+}{\partial x_j^+}} \right), \tag{19}$$

$$\text{Molecular diffusion:} \quad D_{ij} = \frac{\partial^2}{\partial x_k^{+2}} (\overline{u_i'^+ u_j'^+}), \tag{20}$$

$$\text{Dissipation:} \quad \varepsilon_{ij} = 2 \overline{\left(\frac{\partial u_i'^+}{\partial x_k^+} \right) \left(\frac{\partial u_j'^+}{\partial x_k^+} \right)}. \tag{21}$$

Figure 12 shows the budget terms of the Reynolds stresses for $Re_\tau = 640$ compared with those of $Re_\tau = 180$ and 395. For $\overline{u'^+ u'^+}$ component, as the Reynolds number becomes higher, the peak value of the production and the wall values of the molecular diffusion and dissipation increase. The production almost balances with the some of the dissipation and the velocity pressure-gradient correlation (v.p.g, hereafter) terms. On the other hand, for $\overline{v'^+ v'^+}$ and $\overline{w'^+ w'^+}$ components, the v.p.g and dissipation terms are dominant and increase significantly with the increase of the Reynolds number. These indicate that the Reynolds-number effect on $\overline{v'^+ v'^+}$ and $\overline{w'^+ w'^+}$ components is more enhanced than that of $\overline{u'^+ u'^+}$.

Budget terms of turbulent kinetic energy $k(= (\overline{u'^+ u'^+} + \overline{v'^+ v'^+} + \overline{w'^+ w'^+})/2)$ normalized by ν / u_τ^4 are given in Fig. 13 for the three Reynolds numbers calculated. Note that the v.p.g
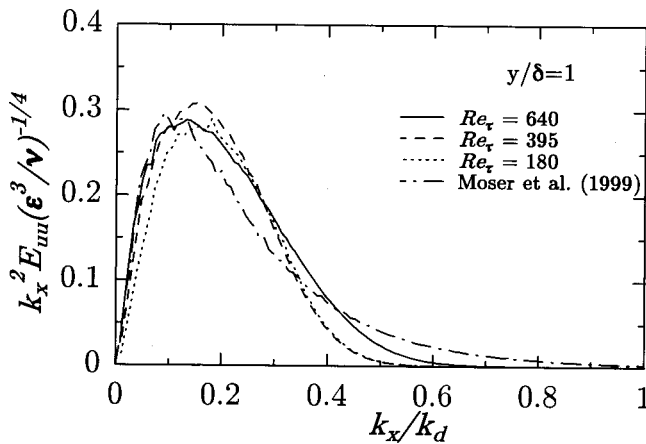
Fig. 9 One-dimensional energy spectra of velocity fluctuations for Re$_\tau$=640 in comparison with Re$_\tau$=180: (a) streamwise, (b) spanwise

term is reduced to the pressure diffusion one due to the continuity condition. Figure 13 indicates that all terms gradually increase with the increase of Re$_\tau$. Especially, the wall values of the dissipation and molecular diffusion increase appreciably with the increasing Reynolds number. The peak value of the production term $P_{k,\max}$ becomes 0.25 as the Reynolds number goes to the infinity. In the present results, $P_{k,\max}$ is 0.218 for Re$_\tau$=180; while, it reaches 0.239 for Re$_\tau$=640. The increase in $P_{k,\max}$ from Re$_\tau$ =180 to 640 is small but significant. This point will be discussed later together with the pressure strain term.
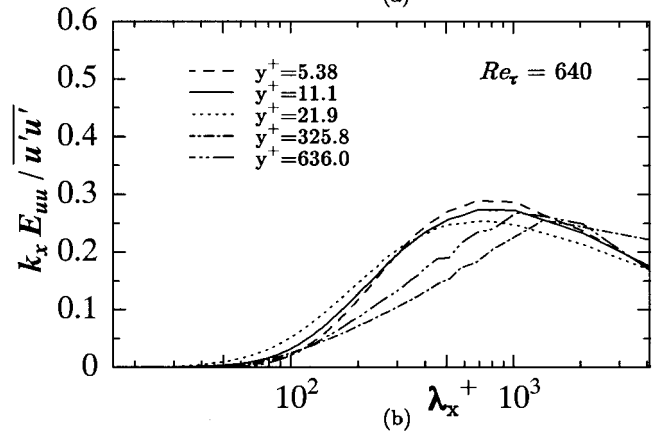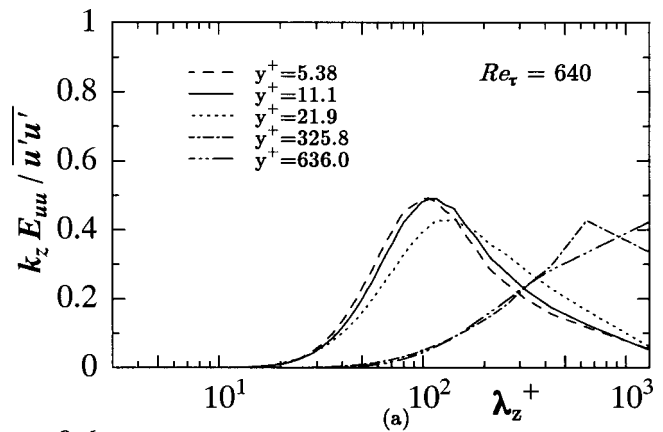
The v.p.g term can be split into the pressure strain and the pressure diffusion terms as follows:

$$\Pi_{ij} = \underbrace{\overline{p'^+ \left(\frac{\partial u_j'^+}{\partial x_i^+} + \frac{\partial u_i'^+}{\partial x_j^+} \right)}}_{\text{Pressure strain}}$$

$$- \underbrace{\left(\frac{\partial}{\partial x_i^+} \overline{u_j'^+ p'^+} + \frac{\partial}{\partial x_j^+} \overline{u_i'^+ p'^+} \right)}_{\text{Pressure diffusion}}. \qquad (22)$$
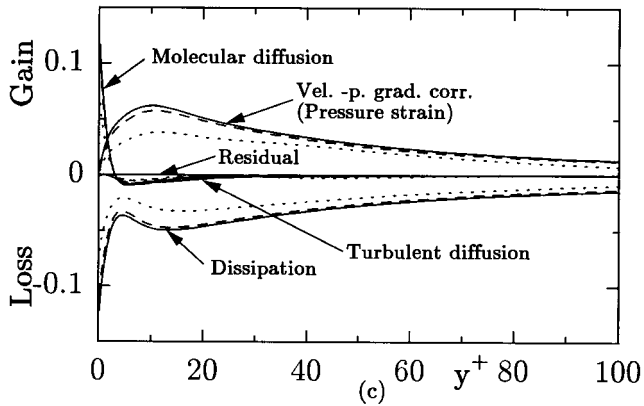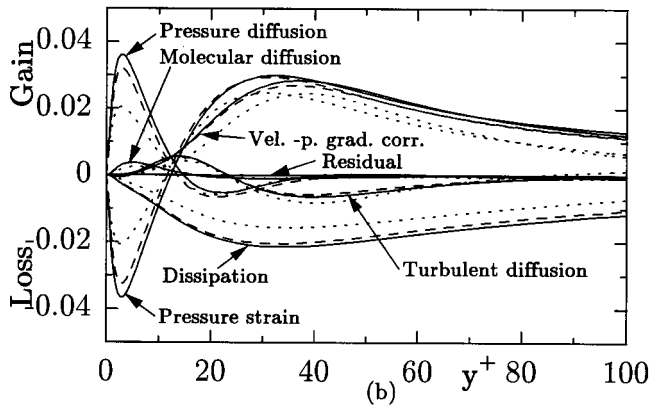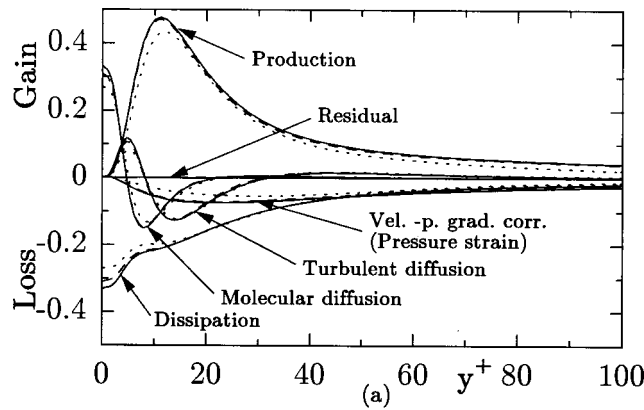
It is well-known that the pressure strain term plays a dominant role on the energy redistribution. Figure 12 indicates that all the components for the pressure strain term exhibit a prominent increase with increasing Reynolds number. It is interesting to note that the increase in the pressure strain of $\overline{u'^+ u'^+}$ from Re$_\tau$
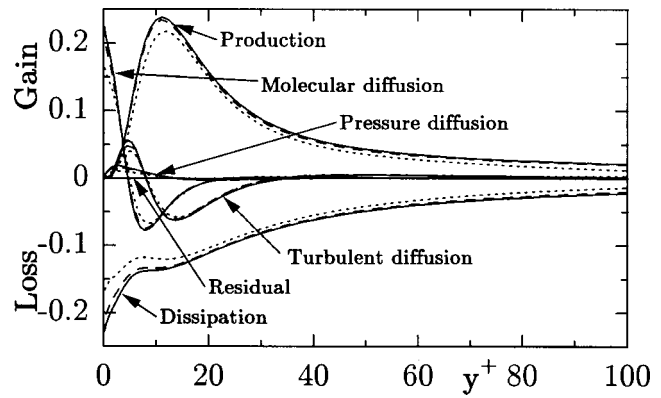

Fig. 10 Streamwise one-dimensional energy dissipation spectra normalized by Kolmogorov scale

Fig. 11 Premultiplied energy spectra for Re$_\tau$=640 (a) $k_z E_{uu}/\overline{u'u'}$, (b) $k_x E_{uu}/\overline{u'u'}$

Fig. 12 Budget of Reynolds normal stresses: (a) $\overline{u'^{+}u'^{+}}$, (b) $\overline{v'^{+}v'^{+}}$, (c) $\overline{w'^{+}w'^{+}}$, ——, Re_{τ}=640; – – –, Re_{τ}=395; - - -, Re_{τ}=180

Fig. 13 Budget of turbulent kinetic energy: ——, Re_{τ}=640; – – –, Re_{τ}=395; - - -, Re_{τ}=180

$$\varepsilon_{(ii)}=\frac{\overline{u_{(i)}'^{+}u_{(i)}'^{+}}}{2k}2\varepsilon. \qquad (23)$$

The present results are compared with the above approximation in Fig. 14. The agreement is generally good for all the normal components. If examined more precisely, however, the agreement is less satisfactory in the central region of $i=1$ and 2 and also in the near-wall region of $i=2$. In the near-wall region, referring to Launder and Reynolds [38], the relation of Eq. (23) is exactly valid for $i=1$ and 3; while, for $i=2$, the wall asymptotic value of ε_{22} becomes
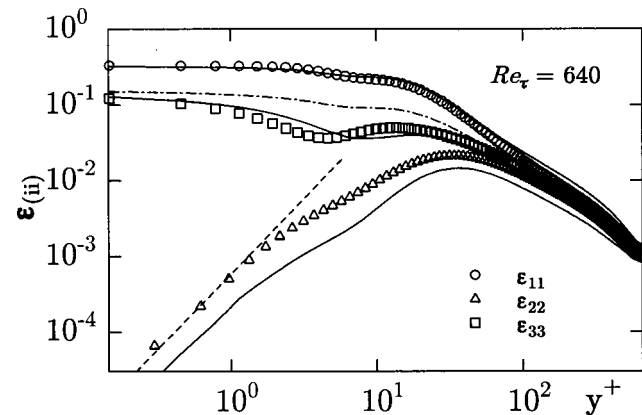
$$\varepsilon_{22}=4c_{2}^{2}y^{+2}, \qquad (24)$$

where c_2 is the expansion coefficient in Eq. (14). The above relation is shown in Fig. 14 with a dashed straight line; the agreement is good in the close vicinity of the wall. The above Eq. (24) is equivalent to

$$\varepsilon_{22}=4\frac{\overline{v'^{+}v'^{+}}}{2k}2\varepsilon, \qquad (25)$$

instead of Eq. (23). This is one reason why the agreement of Eq. (23) is not so good for $i=2$ as seen in Fig. 14.

To examine the above approximation further, the anisotropy tensors are defined for the Reynolds stress and its dissipation rate as follows:

=180–640 is about 0.02 around its peak. This value is roughly equal to the increase in the peak of P_k. Since P_k is a half of the P_{11}, it means that about half of the increase in the production rate of $\overline{u'^{+}u'^{+}}$ is consumed by $\overline{u'^{+}u'^{+}}$ itself and the rest half is transferred to the other components. This is the reason why v'^{+}_{rms} and ω'^{+}_{rms} increase significantly with the increase of the Reynolds number.

Dissipation Rate of the Reynolds Stresses. The dissipation rate of the Reynolds stresses is the quantity obtained best from DNS. The anisotropy of the dissipation rate for the normal Reynolds stress components is of a great concern in the modeling of turbulence. Mansour et al. [37] examined the DNS data of KMM87 [2] for Re_{τ}=180 and found that the following expression is a good approximation except for the off-diagonal components:

Fig. 14 Dissipation rate of the normal Reynolds stresses for Re_{τ}=640 symbol, $\varepsilon_{(ii)}$ by Eq. (23); ——, $\overline{u_{(i)}'^{+}u_{(i)}'^{+}}(\varepsilon/k)$; —·—·—·—, $(2/3)\varepsilon$; – – –, $4c_{2}^{2}y^{+2}$
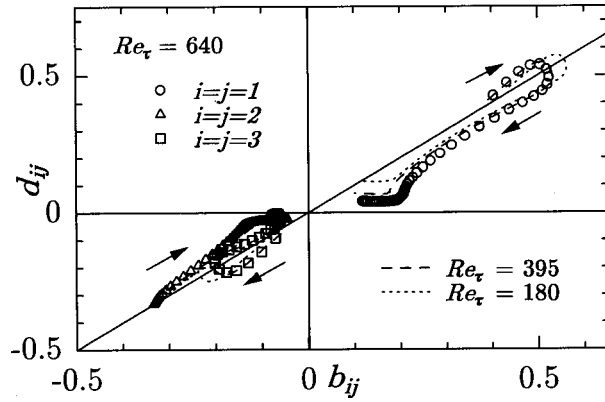
Fig. 15 Relation between anisotropy tensors b_{ij} and d_{ij}

$$b_{ij} = \frac{\overline{u_i'^+ u_j'^+}}{2k} - \frac{\delta_{ij}}{3}, \qquad (26)$$

$$d_{ij} = \frac{\varepsilon_{ij}}{2\varepsilon} - \frac{\delta_{ij}}{3}. \qquad (27)$$

Antonia et al. [39] compared the relation between b_{ij} and d_{ij} for a turbulent boundary layer. The same kind of comparison is made here for the turbulent channel flow in Fig. 15. For the above approximation of Eq. (23) to be exactly valid, the equality $d_{ij} = b_{ij}$ must hold. The arrows in Fig. 15 indicate the direction from the wall to the channel center. The starting point (wall value) lies on the line of $d_{ij} = b_{ij}$; especially $b_{ij} = d_{ij} = -1/3$ for $i = j = 2$. The relation of $d_{ij} = b_{ij}$ holds roughly for the whole region. It is, however, interesting to note that d_{ij} becomes parallel to the horizontal axis where the absolute value of b_{ij} is small. This means that the dissipation becomes nearly isotropic irrespective of the Reynolds stress anisotropy in the central region. This supports the well-known belief that the dissipation must be almost isotropic because it takes place in the microscale, which is more isotropic than the large scale eddies. The isotropic expression

$$\varepsilon_{(ii)} = \frac{2}{3}\varepsilon \qquad (28)$$

is plotted with the dot-dashed line in Fig. 14. This is indeed in a better agreement than Eq. (23) in the central region.

Instantaneous Flow Field. A lot of knowledge has been accumulated for the turbulent structures through the experimental observation and the analysis of the DNS data. In the present study, we focus mainly on the Reynolds number dependence for the quasi-coherent structures such as vortices and streaks. Figures 16 and 17 show the high- and low-speed streaks and the second invariant of the deformation tensor ($II' = \partial u_i'/\partial x_j \cdot \partial u_j'/\partial x_i$) for $Re_\tau = 180$ and 640. The visualized domain is set in wall units to be $1152 \times 180 \times 576$ for $Re_\tau = 180$ and $2048 \times 640 \times 640$ for $Re_\tau = 640$ in x, y and z directions, respectively. Note that fluid flows from the bottom left to the top right.

Chong et al. [40] proposed the identification of the vortex region which exhibits the circular or spiral motion with using the second invariant of the deformation tensor. The low pressure region (p'^+) does not necessarily correspond to the vortex core as indicated by Kim [41] and Robinson [42]. Thus, the second invariant of the deformation tensor is adopted to detect the vortex structure in the present research. When the Reynolds number is low as $Re_\tau = 180$, the well-known vortex structures such as single quasi-streamwise vortices are dominant. On the other hand, as the Reynolds number increases up to $Re_\tau = 640$, many different vortical structures such as the vortical arches are found besides the single streamwise vortices. The vortical arches are rolled up over
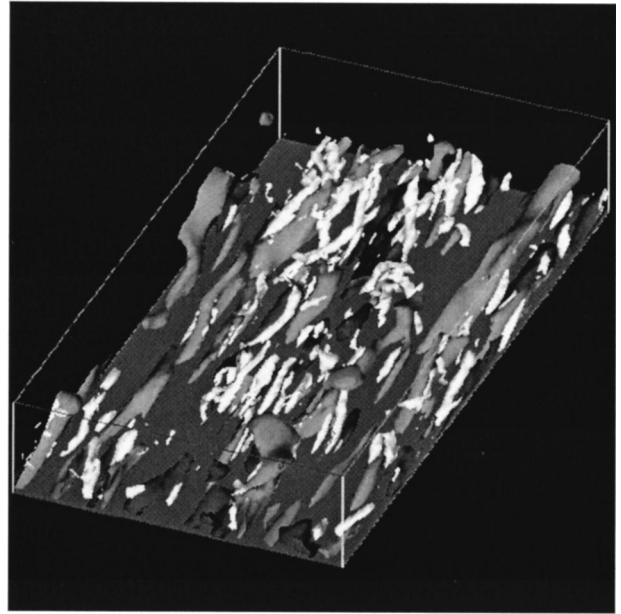

Fig. 16 High- and low-speed streaks and the second invariant of the deformation tensor for $Re_\tau=180$ ($u'^+<-3.0$; light-gray, $u'^+>3.0$; dark-gray, $II'^+<-0.03$; white)

the low-speed streaks. Other vortices including the single streamwise vortices are also associated closely with the low-speed streaks.

As for the streaks, high- and low-speed streaks are obtained for both Re_τ's. The low-speed streaks are more elongated than the high-speed ones for both of the Reynolds numbers observed. The spanwise two-point correlation R_{11} is generally used to estimate the spacing of the streaks. It is known that the position of the negative peak of R_{11} provides an estimation of the mean separation between the high- and low-speed streaks; that is, the streak spacing becomes twice of the distance to the negative peak. KMM87 [2] obtained the minimum value of R_{11} at $z^+ \simeq 50$ and
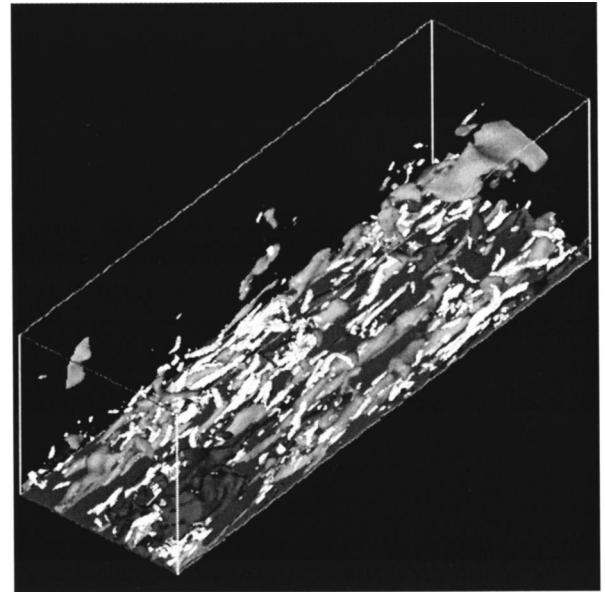

Fig. 17 High- and low-speed streaks and the second invariant of the deformation tensor for $Re_\tau=640$ ($u'^+<-3.0$; light-gray, $u'^+>3.0$; dark-gray, $II'^+<-0.03$; white)

indicated that the streak spacing was $\Delta z^+ \simeq 100$, with which the present DNS for $\text{Re}_\tau = 180$ gives a good agreement as shown in Fig. 16. Comparison of Figs. 16 and 17 indicates that the separation of the high- and low-speed streaks is more prominent in the lower Reynolds number and less in the higher one. That is, in case of $\text{Re}_\tau = 640$, the shape of the streaks becomes more complicated and the several streaks are clustered with each other. Moreover, several low-speed streaks are often lifted up from the wall and finally broken up (see Fig. 17). This observation is in agreement with the finding that the local minimum of the R_{11} becomes less prominent with the increase of the Reynolds number as seen in Fig. 8.

Conclusions

The direct numerical simulation of a fully developed turbulent channel flow has been carried out. The Reynolds number is set to be $\text{Re}_\tau = 180$, 395, and 640. The computation has been executed with the use of the finite difference method. Various turbulence statistics, such as turbulence intensities, vorticity fluctuations, Reynolds stresses, their budget terms, two-point correlation coefficients and energy spectra, were obtained to investigate the Reynolds number dependence. The conclusions are derived as follows:

1 With the increase of Re_τ, the increase in the wall-normal ($v_{\text{rms}}'^+$) and spanwise ($w_{\text{rms}}'^+$) components is more enhanced than that of the streamwise one ($u_{\text{rms}}'^+$). About half of the increase in the production rate of $\overline{u'^+ u'^+}$ is consumed by $\overline{u'^+ u'^+}$ and the rest half is transferred to the other components.

2 The near-wall expansion coefficients increase significantly as the Reynolds number goes up from $\text{Re}_\tau = 180$– 395, but become rather saturated for $\text{Re}_\tau = 640$. The wall-limiting value of b_1 obtained as 0.409 agrees with the experiment for the channel flow by Alfredsson and Johansson [33] and the DNS for the Couette flow by Komminaho et al. [34].

3 The examination of the spanwise two-point correlation coefficient R_{11} reveals that the negative peak of R_{11} becomes less prominent with the increase of the Reynolds number. This agrees with the more complex streak shapes observed in the instantaneous velocity field for the higher Reynolds number.

4 The dissipation energy spectra $k_x^2 E_{uu}(\varepsilon^3/\nu)^{-1/4}$ in the center of the channel exhibits a peak value at $k_x/k_d = 0.1 - 0.2$ and falls off for $k_x/k_d > 0.5$ irrespective of the Reynolds numbers calculated as indicated by the local isotropic theory (Tennekes and Lumley [36]).

5 The anisotropy of the dissipation rate for the Reynolds normal stresses is compared with closure models. The anisotropy is pronounced in the wall vicinity; while the well-known isotropic nature is confirmed in the central region for a higher Reynolds number.

6 The second invariant of the deformation tensor represents the vortices such as the single streamwise vortices and the vortical arches for $\text{Re}_\tau = 640$. In addition, different vortical structures are captured with the increase of the Reynolds number. As for the streaks, rather simple and separated streaky structures are observed for the lower Reynolds number of $\text{Re}_\tau = 180$; while, the shape of the streaks becomes more complicated and several streaks are clustered with each other for the higher Reynolds number of $\text{Re}_\tau = 640$.

The present database is open to public access. The detailed information is given at http://muraibm.me.noda.sut.ac.jp/e-pagel.html.

Acknowledgments

Nomenclature

b_i, c_i, d_i = coefficient of series expansion
b_{ij} = anisotropy tensor of Reynolds stress
C_f = friction coefficient
c = additive constant of the logarithmic law
d_{ij} = anisotropy tensor of dissipation rate
E_{ij} = one-dimensional energy spectra of velocity fluctuations
k = turbulent kinetic energy
k_x, k_z = wave number for streamwise and spanwise direction
k_d = Kolmogorov wave number
p = pressure
P_k = production rate for the turbulent kinetic energy
R_{ii} = two-point correlation coefficient of velocity fluctuations
Re_τ = Reynolds number$= u_\tau \delta/\nu$
Re_m = Reynolds number$= u_m 2\delta/\nu$
Re_c = Reynolds number$= u_c \delta/\nu$
Re_θ = Reynolds number$= u_c \theta/\nu$
t = time
u_i, u, v, w = velocity component
u_τ = friction velocity$= \sqrt{\tau_w/\rho}$
u_c = mean centerline velocity
u_m = bulk mean velocity
u_∞ = edge velocity of the turbulent boundary layer
x_1, x = streamwise direction
x_2, y = wall-normal direction
x_3, z = spanwise direction

Greek

δ = channel half width
δ_{ij} = Kroneker symbol
ε = dissipation rate of turbulent kinetic energy
ε_{ii} = dissipation rate of Reynolds stress
κ = von Karman constant
θ = momentum thickness
ν = kinematic viscosity
ω_i = vorticity component
ρ = density
λ_x, λ_z = wavelength for streamwise and spanwise direction
τ_w = statistically averaged wall shear stress
τ_{total} = statistically averaged total shear stress

Superscripts and Subscripts

$(\ )^*$ = normalized by δ
$(\ )^+$ = normalized by u_τ, ν and ρ
$(\ )'$ = fluctuationcomponent
$(\bar{\ })$ = statistically averaged over x, z, and t
$(\ )_{\text{rms}}$ = root mean square
$(\ )_{\text{max}}$ = maximum value

Appendix

A. Consistent Scheme. The convection terms for u_i can be expressed in either advective ($\text{adv.} \equiv u_j \partial u_i/\partial x_j$) or divergence ($\text{div.} \equiv \partial/\partial x_j u_i u_j$) forms. Since

$$\frac{\partial}{\partial x_j} u_i u_j = u_j \frac{\partial u_i}{\partial x_j} + u_i \frac{\partial u_j}{\partial x_j}, \tag{29}$$

the advective and divergence forms are analytically equal if the continuity condition is satisfied. Thus, this equality must be satis-
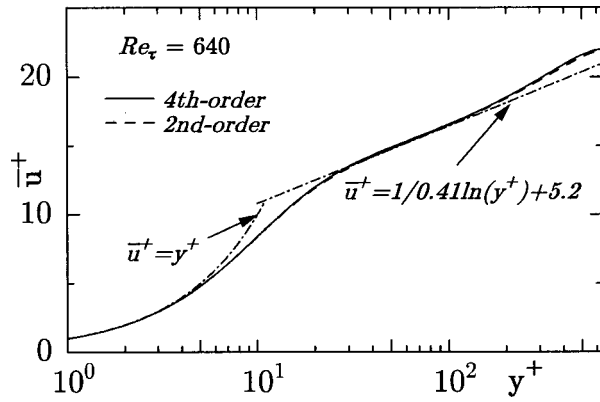
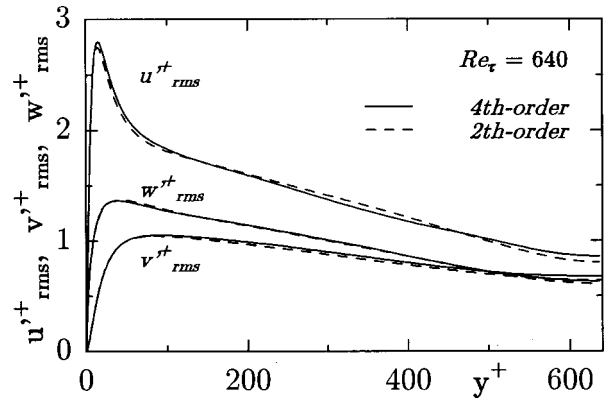**Fig. 18 Mean velocity distribution by fourth-order calculation**

Fig. 19 Rms of velocity fluctuations by fourth-order calculation
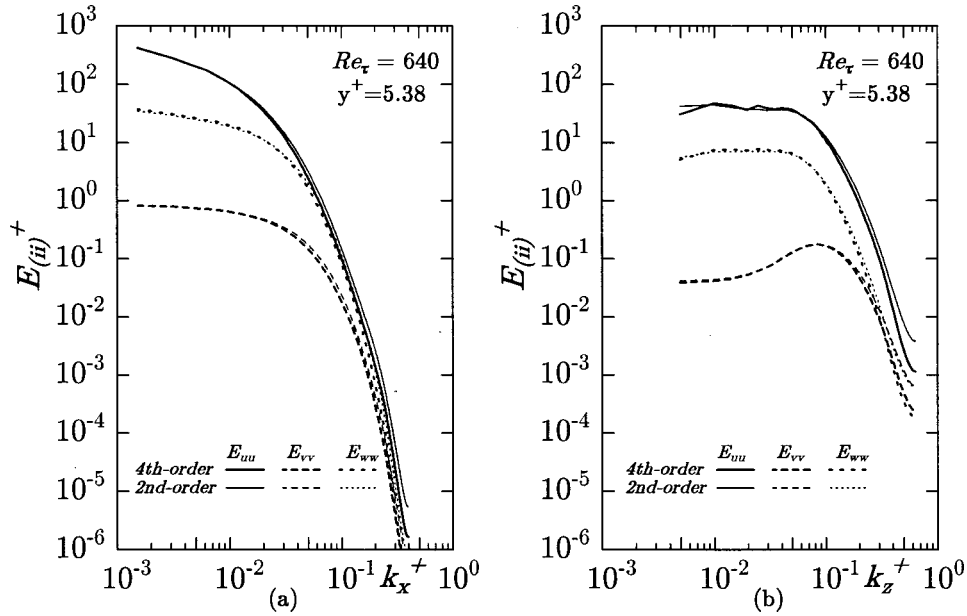

Fig. 20 One-dimensional energy spectra of velocity fluctuations by fourth-order calculation: (a) streamwise, (b) spanwise

fied in the numerical discretized scheme, too. This is the consistency between the analytical and numerical differential operations.

In the present computational stencil, the staggered grid is adopted; that is, the pressure is located at the cell center and the velocities at the cell surfaces.

The following difference operation is defined referring to Morinishi [30]

$$\frac{\delta \phi}{\delta x_1} = \frac{\phi(x_1 + h_1/2, x_2, x_3) - \phi(x_1 - h_1/2, x_2, x_3)}{h_1}, \quad (30)$$

where ϕ is a variable in the x_1 direction. Interpolation operator is given as

$$\overline{\phi}^{x_1} = \frac{1}{2}(\phi(x_1 + h_1/2, x_2, x_3) + \phi(x_1 - h_1/2, x_2, x_3)). \quad (31)$$

Moreover, a special interpolation of the variables between ϕ and ψ in the x_1 direction is expressed as

$$\overline{\phi\psi}^{x_1} \equiv \frac{1}{2} \phi(x_1 + h_1/2, x_2, x_3) \psi(x_1 - h_1/2, x_2, x_3)$$

$$+ \frac{1}{2} \psi(x_1 + h_1/2, x_2, x_3) \phi(x_1 - h_1/2, x_2, x_3). \quad (32)$$

The present numerical discretization is based on the second accuracy (Kawamura [26]; Suzuki and Kawamura [27]) and defined as follows.

The discretized continuity equation can be expressed as

$$(\text{Cont.}) \equiv \frac{\delta u_i}{\delta x_i} = 0. \quad (33)$$

For the convective terms, the advective and divergence forms are discretized as

$$(\text{Adv.})_i \equiv \overline{\overline{u_j}^{x_i} \frac{\delta u^i}{\delta x_j}}^{x_j}, \quad (34)$$

and

$$(\text{Div.})_i \equiv \dfrac{\overline{\dfrac{\delta u_j}{}}^{\,x_i} u_i}{\delta x_j}.$$

$$\dfrac{\overline{\delta u_j}^{x_i}\, \overline{u_i}^{x_j}}{\delta x_j}. \tag{35}$$

One can easily confirm that these forms are connected with the following relation:

$$(\text{Adv.})_\alpha = (\text{Div.})_\alpha - u_\alpha \cdot \overline{(\text{Cont.})}^{\,1x_\alpha}, \tag{36}$$

where the summation convention is not applied to the suffix α. Equation (36) corresponds to the analytical equality of Eq. (29). Therefore, the discretized scheme becomes independent of the above forms within the numerical accuracy of the continuity equation (Eq. (33)). In the present computation, the advective form is adopted for the convective terms. Similar numerical operations have also been devised to calculate the budget terms of the Reynolds stress transport equations with retaining the consistency.

B. Fourth-Order Calculation. To examine the numerical accuracy of the present calculation, the fourth-order scheme proposed by Morinishi [30] is adopted in the x and z directions for spatial discretization. The rest of the calculation method is the same as the one adopted in the text. The Reynolds number is set to be $\text{Re}_\tau = 640$.

The mean velocity distribution and the root mean square of the velocity fluctuations are shown in Figs. 18 and 19, respectively. The results by the fourth-order scheme are in agreement with those by the second-order one in the whole region. The small discrepancy, however, is observed in the channel center region for the turbulence intensities, but it is not significant.

One-dimensional energy spectra of velocity fluctuations $E_{(ii)}$ are given in Fig. 20 in comparison with that of the second-order scheme. In the streamwise energy spectra, no significant difference can be found between the second- and fourth-order schemes. In the spanwise energy spectra, on the other hand, a noticeable difference can be seen in the highest wave numbers. These wave numbers are, however, already beyond the peak of the dissipation spectra; thus the effect is not so significant so long as higher-order correlations and derivatives are not concerned.

For the results, it can be concluded that the mean properties and the second moment correlations can be captured even by the second-order scheme with the present grid resolution. This conclusion, as a matter of course, depends upon the grid resolution. In the case of DNS, however, an enough fine grid is adopted inevitably to capture the finest scale of turbulence. This is the reason why the acceptable results can be obtained even with the second-order scheme.

References

[1] Orszag, S. A., and Patterson, G. S., 1972, ''Numerical simulation of three-dimensional homogeneous isotropic turbulence,'' Phys. Rev. Lett., **28**, pp. 76–79.

[2] Kim, J., Moin, P., and Moser, R., 1987, ''Turbulence statistics in fully developed turbulent channel flow at low Reynolds number,'' J. Fluid Mech., **177**, pp. 133–166.

[3] Kuroda, A., Kasagi, N., and Hirata, M., 1989, ''A direct numerical simulation of the fully developed turbulent channel flow at a very low Reynolds number,'' Int. Symp. Computational Fluid Dynamics, Nagoya, pp. 1174–1179.

[4] Kasagi, N., Tomita, Y., and Kuroda, A., 1992, ''Direct numerical simulation of passive scalar field in a turbulent channel flow,'' ASME J. Heat Transfer, **114**, pp. 598–606.

[5] Kim, J., Moin, P., and Moser, R., 1990, The Diskette of Collaborative Testing of Turbulence Models, Bradshaw, P., ed., Stanford University.

[6] Antonia, R. A., and Kim, J., 1994, ''Low-Reynolds-number effects on near-wall turbulence,'' J. Fluid Mech., **276**, pp. 61–80.

[7] Kawamura, H., Ohsaka, K., Abe, H., and Yamamoto, K., 1998, ''DNS of turbulent heat transfer in channel flow with low to medium-high Prandtl number fluid,'' Int. J. Heat and Fluid Flow, **19**, pp. 482–491.

[8] Kawamura, H., Abe, H., and Matsuo, Y., 1999, ''DNS of turbulent heat transfer in channel flow with respect to Reynolds and Prandtl number effects,'' Int. J. Heat and Fluid Flow, **20**, pp. 196–207.

[9] Kawamura, H., 1998, ''Direct numerical simulation of turbulence by parallel computation,'' Proc. 10th Int. Conf. Parallel CFD, pp. 19–21.

[10] Kawamura, H., Abe, H., and Matsuo, Y., 1999, ''Direct numerical simulation of turbulence by parallel computation,'' Parallel Computational Fluid Dynamics, Lin et al., eds., North-Holland, Amsterdam, pp. 3–9.

[11] Moser, R. D., Kim, J., and Mansour, N. N., 1999, ''Direct numerical simulation of turbulent channel flow up to Re$_\tau$=590,'' Phys. Fluids, **11**, pp. 943–945.

[12] Laufer, J., 1951, ''Investigation of turbulent flow in a two-dimensional channel,'' NACA Rept., Vol. 1053, pp. 1247–1266.

[13] Hussain, A. K. M. F, and Reynolds, W. C., 1975, ''Measurements in fully developed turbulent channel flow,'' ASME J. Fluids Eng., **97**, pp. 568–580.

[14] Kreplin, H. P., and Eckelmann, H., 1979, ''Behavior of the three fluctuating velocity components in the wall region of a turbulent channel flow,'' Phys. Fluids, **22**, pp. 1233–1239.

[15] Johansson, A. V., and Alfredsson, P. H., 1982, ''On the structure of turbulent channel flow,'' J. Fluid Mech., **122**, pp. 295–314.

[16] Wei, T., and Willmarth, W. W., 1989, ''Reynolds-number effects on the structure of a turbulent channel flow,'' J. Fluid Mech., **204**, pp. 57–95.

[17] Antonia, R. A., Teitel, M., Kim, J., and Browne, L. W., 1992, ''Low-Reynolds-number effects in a fully developed turbulent channel flow,'' J. Fluid Mech., **236**, pp. 579–605.

[18] Nishino, K., and Kasagi, N., 1989, ''Turbulence statistics measurement in a two-dimensional channel flow using a three-dimensional particle tracking velocimeter,'' Proc. 7th Turbulent Shear Flows, Vol. 2, pp. 22.1.1–22.1.6.

[19] Nishino, K., and Kasagi, N., 1991, ''On the quasi-coherent turbulence structures in the two-dimensional channel flow,'' Proc. 8th Turbulent Shear Flows, Vol. 2, pp. 28.3.1–28.3.6.

[20] Moin, P., and Kim, J., 1982, ''Numerical investigation of turbulent channel flow,'' J. Fluid Mech., **118**, pp. 341–377.

[21] Jiménez, J., 1998, ''The largest scales of turbulent wall flows,'' Center for Turbulence Research Annual Research Briefs, pp. 137–154.

[22] Dukowics, J. K., and Dvinsky, A. S., 1992, ''Approximate factorization as a high order splitting for the implicit incompressible flow equations,'' J. Comput. Phys., **102**, pp. 336–347.

[23] Rai, M. M., and Moin, P., 1991, ''Direct simulation of turbulent flow using finite-difference schemes,'' J. Comput. Phys., **96**, pp. 15–53.

[24] Rai, M. M., and Moin, P., 1993, ''Direct numerical simulation of transition and turbulence in a spatially evolving boundary layer,'' J. Comput. Phys., **109**, pp. 169–192.

[25] Gavrilakis, S., 1992, ''Numerical simulation of low-Reynolds-number turbulent flow through a straight square duct,'' J. Fluid Mech., **244**, pp. 101–129.

[26] Kawamura, H., 1994, ''Direct numerical simulation of turbulence by finite difference scheme,'' The Recent Developments in Turbulence Research, Z. S. Zhang and Y. Miyake, eds. International Academic Publishers, pp. 54–60.

[27] Suzuki, T., and Kawamura, H., 1994, ''Consistency of finite-difference scheme in direct numerical simulation of turbulence (in Japanese),'' Trans. JSME, **60−578B**, pp. 3280–3286.

[28] Schumann, U., 1975, ''Subgrid scale model for finite difference simulations of turbulent flows in plane channels and annuli,'' J. Comput. Phys., **18**, pp. 376–404.

[29] Kajishima, T., 1994, ''Conservation properties of finite difference method for convection (in Japanese),'' Trans. JSME, **60−574B**, pp. 2058–2063.

[30] Morinishi, Y., 1995, ''Conservative properties of finite difference scheme for incompressible flow,'' Center for Turbulence Research Annual Research Briefs, pp. 121–132.

[31] Spalart, P. R., 1988, ''Direct simulation of a turbulent boundary layer up to R_θ=1410,'' J. Fluid Mech., **187**, pp. 61–98.

[32] Dean, R. B., 1978, ''Reynolds number dependence of skin friction and other bulk flow variables in two-dimensional rectangular duct flow,'' ASME J. Fluids Eng., **100**, pp. 215–222.

[33] Alfredsson, P. H., and Johansson, A. V., 1988, ''The fluctuating wall-shear stress and the velocity field in the viscous sublayer,'' Phys. Fluids, **31**, pp. 1026–1033.

[34] Komminaho, J., Lundbladh, A., and Johansson, A. V., 1996, ''Very large structures in plane turbulent Couette flow,'' J. Fluid Mech., **320**, pp. 259–285.

[35] Saddoughi, S. G., and Veeravalli, S. V., 1994, ''Local isotropy in turbulent boundary layers at high Reynolds number,'' J. Fluid Mech., **268**, pp. 333–372.

[36] Tennekes, H., and Lumley, J. L., 1972, A First Course in Turbulence, MIT Press, Cambridge, MA.

[37] Mansour, N. N., Kim, J., and Moin, P., 1988, ''Reynolds-stress and dissipation-rate budgets in a turbulent channel flow,'' J. Fluid Mech., **194**, pp. 15–44.

[38] Launder, B. E., and Reynolds, W. C., 1983, ''Asymptotic near-wall stress dissipation rates in a turbulent flow,'' Phys. Fluids, **26**, p. 1157.

[39] Antonia, R. A., Djenidi, L., and Spalart, P. R., 1994, ''Anisotropy of the dissipation tensor in a turbulent boundary layer,'' Phys. Fluids, **6**, pp. 2475–2479.

[40] Chong, M. S., Perry, A. E., and Cantwell, B. J., 1990, ''A general classification of three-dimensional flow fields,'' Phys. Fluids A, **4**, pp. 765–777.

[41] Kim, J., 1989, ''On the structure of pressure fluctuations in simulated turbulent channel flow,'' J. Fluid Mech., **205**, pp. 421–451.

[42] Robinson, S. K., 1991, ''The kinematics of turbulent boundary layer structure,'' NASA TM, 103859.